Toxicology Reports 5 (2018) 468–479

Contents lists available at ScienceDirect

Toxicology Reports

journal homepage: www.elsevier.com/locate/toxrep

Influence of formulation of ZnO nanoblokes containing metallic ions dopants on their cytotoxicity and protective factors: An in vitro study on human skin cells exposed to UVA radiation

Parvaneh Ghaderi-Shekhi Abadi[a,b], Farshad H. Shirazi[c], Mohammad Joshaghani[b,d], Hamid R. Moghimi[a,e,*]

[a] Department of Pharmaceutics and Nanotechnology, School of Pharmacy, Shahid Beheshti University of Medical Sciences, Tehran, Iran
[b] Institute of Nanoscience and Nanotechnology, Razi University, Kermanshah, Iran
[c] Pharmacology and Toxicolgoy, School of Pharmacy, Shahid Beheshti University of Medical Sciences, Tehran, Iran
[d] Department of Inorganic Chemistry, Faculty of Chemistry, Razi University, Kermanshah, Iran
[e] Protein Technology Research Center, Shahid Beheshti University of Medical Sciences, Tehran, Iran

ARTICLE INFO

Keywords:
Metal-promoted Zn-based nanocomposite
Safe ZnO nanoparticles
Human skin cells
UVA radiation
Cytotoxicity and protective effects

ABSTRACT

Application of ZnO nanoparticles in sunscreens exposes human skin with their adverse effects, which correlates to dissolution/translocation of free Zn^{+2} ions. The possibility of decreasing solubility and therefore, reducing toxicity, by structural modifications have been discussed as a solution. The present investigation has developed new metallic lattices of ZnO to reduce cytotoxicity of ZnO nanoparticles. Novel metal-promoted Zn-based nanocomposites ([Zn(O)/M], M = Mg, Al, Ca, Ti) were synthesized and their physicochemical properties and their cytotoxicity were evaluated. Solubility and release studies showed that modification of ZnO structure decreases release of Zn^{+2} into culture medium. XRD and UV absorbance analyses showed that metallic-dopants percolate into crystalline lattice of ZnO. This phenomenon is basic reason for stability of Zn-based network. Cell culture studies and MTT assay on human skin cells (HFF-1) exposed to UVA radiation showed that the level of protection of [Zn(O)/M] compounds were more than of [ZnO]. Dichlorofluoroscein diacetate-ROS assay and Zn^{+2} release experiments indicated that [Zn(O)/M] nanocomposites decreased the level of ROS generation and Zn^{+2} release in compared to ZnO, indicating higher safety of nanocomposites. This study shows that the synthesized Zn-based nanocomposites have potential to be used as safer and more effective sunscreens than ZnO.

1. Introduction

Exposure of human skin with sunlight and therefore UVA, UVB, and UVC radiations, is the major environmental factor that affects the structure of skin and develops skin cancers. Ozone layer efficiently absorbs UVC and 95% of UVB [1]. The UV radiation generates reactive oxygen species-ROS by photochemical interactions and lead to DNA, proteins, and lipids damages [2–4]. Public health authorities recommend the use of sunscreens, including ZnO, to limit sun light (UVA and UVB radiation) damages [5].

ZnO compounds are interesting class of semiconductor compounds which have been used in sunscreens because of their ability to filter ultraviolet UVA and UVB light. In recent years, manufacturers have started using nano-sized forms of these metal oxide in sunscreens [6]. These new formulation resolved the problem of the unsightly white film of traditional sunscreens and created a vehicle that is more transparent, less viscous, and blends into the skin more easily [7]. With the rapidly increasing application of ZnO particles, several growing community and scientific concern warned to increased health and environmental risks of metallic nanoparticles due to interactions and release of them in the environment and microorganism [8].

Previous reports have shown that nano-ZnO exerts toxicity in mammalian cells as a result of particle dissolution in the tissue culture medium [9,10]. Zn^{+2} ions release in intracellular space induce generation of ROS and cell death [11,12]. Oppositely, some metal nanoparticles may show more toxicity than either their ionic forms or their parent compounds [13]. More soluble compounds like ZnO and FeO show greater acute toxicity than nanoparticles with extremely low solubility such as CeO_2 and TiO_2 [14]. An increasing number of research articles have focused on the cytotoxicity of different types of engineered nanomaterials via the generation of ROS [15,16].

Modifying structure of ZnO nanoparticles is a suitable way for

* Corresponding author at: School of Pharmacy, Shahid Beheshti University of Medical Sciences, Valiasr Ave., Niayesh Junction, PO Box 14155-6153, Tehran, Iran.
E-mail address: hrmoghimi@sbmu.ac.ir (H.R. Moghimi).

https://doi.org/10.1016/j.toxrep.2018.03.001
Received 18 November 2017; Received in revised form 23 February 2018; Accepted 5 March 2018
Available online 06 March 2018

promoting their properties. Over the past decade, it has been shown that Zn-based nanomaterials with multi-metallic structures (Zn(O)-M, M = secondary metal) show new and effective interesting properties that were not seen in mono-metallic structures (ZnO) [17–22]. Previous reports have shown that altering the ZnO matrix through iron doping decreases particle dissolution in tissue culture media and leading to a reduction its toxicity [9]. Also, the synergetic effects of the Cu/Zn bimetallic nanoparticles distributed in the ACFs/CNFs (activated carbon fibres/carbon nanofibres) resulted from the relatively slower release of the Cu nanoparticles located at the tip of the CNFs and faster release of the Zn nanoparticles dispersed in the ACF at the in-vitro hemolytic test [23].

The doping metal on ZnO particles, helps stabilizing both structure and surface morphology of ZnO particles by preventing the release of Zn^{+2} ions in solution [17,24,25]. Incorporation of doping element into ZnO crystal can change lattice parameters and defects (intrinsic/extrinsic) concentration [26–28]. For example, incorporation of metal ions in the semiconductor networks can lead to the formation of electron trapping sites and promote charge transfer from ZnO to metal ions, thus resulting in the enhanced photoreaction of surface adsorbed species [29,30]. With doping of nonmetal ions (e.g., N, S, C, F, etc.) into ZnO lattice, dopants create intra-band-gap states close to the conduction or valence band edges that induce visible light absorption. Unlike metal ions, nonmetal ions are less likely to form recombination centers, and thus are more effective in enhancing visible light activity [31].

Therefore, the multi-metallic nanoparticle not only retains most of the properties of the individual nano-metals but also possess several superior physicochemical properties which could prove beneficial for human health [32–34]. This strategy is employed here to synthesis safer ZnO nanoparticles. In spite of the considerable research into the potential hazardous effects of ZnO bulk- and nano-particles under environmental and biological conditions, attempts have not been made to design a potentially safer ZnO compound. Therefore, it was decided here to develop bimetallic novel heterometallic Zn-based nanocomposites ([Zn(O)/M], M = Mg, Al, Ca, Ti) via thermal method. The effects of metal-doping Zn-based nanocomposites on the solubility, release, UV-blocking behavior, cytotoxicity, and protective effects of them on cultured human skin (HFF-1) cells exposed with UVA radiation were then investigated.

To date, two approaches have been developed to synthesis metal doping ZnO: direct doping method of partial replacement of zinc by either Group I elements such as Na [35], K [36], Li [37] or oxygen by Group V elements such as: N [38], P [39], As [40], and Sb [41]. To the best of our knowledge, there is no report on the fabrication of [Zn(O)/M] (M = Mg, Al, Ca, Ti) nanocomposites and investigation of cytotoxicity and protective effects of them on human skin cells.

2. Materials and methods

2.1. Materials

$CaCl_2{\cdot}2H_2O$ (CAS number (CN): 10035-04-8), $MgCl_2{\cdot}6H_2O$ (CN: 7791-18-6), $AlCl_3$ (CN: 7446-70-0), $TiCl_4$ (CN: 7550-45-0), polyethylene glycol (PEG, M.W. = 35000 g/mol, CN: 25322-68-3), 1-Hexadecyltrimethylammonium bromide (CTAB, ≥98%, CN: 57-09-0), absolute ethanol (CN: 64-17-5), and dimethyl sulfoxide (DMSO, CN: 67-68-5) were purchased from Merck, Germany. $Zn(OAc)_2{\cdot}2H_2O$ (CN: 5970-45-6, ≥99.99%), commercial ZnO (nanoparticle morphology, CN: 1314-13-2), hydrazinium hydroxide (65 wt%, CN: 7803-57-8), 2′,7′-dichlorodihydrofluorescein diacetate (DCFH-DA, ≥97%, CN: 4091-99-0), phosphate-buffered saline (PBS), Dulbecco's Modified Eagle's Medium (DMEM), fetal bovine serum (FBS), 3-(4,5-dimethyl-2-thiazolyl)-2,5-diphenyl-2H-tetrazolium bromide (MTT, CN: 298-93-1), and cellulose dialysis tube were purchased from Sigma-Aldrich, USA. Normal saline (NS) and lansulin were purchased from Exir Pharmaceutical Company, Iran. Penicillin was purchased from Jabiribn Hayyan Pharmaceutical Company, Iran. All compounds were purchased with analytical grades and these were used without further purification.

2.2. Preparation of the metal-doping Zn-based nanocomposites

In a typical synthesis, 0.02 g paraffin was dissolved in 2 mL ultrapure water at 50 °C (solution 1). After 5 min, 0.05 mmol CTAB was added to solution 1. In a separate beaker, 4.50 mmol $Zn(OAc)_2{\cdot}2H_2O$ was dissolved in 4 mL ultrapure water (solution 2). 0.50 mmol chloride salt ($CaCl_2$, $MgCl_2{\cdot}6H_2O$, $AlCl_3$, $TiCl_4$) was dissolved separately in 2 mL of ultrapure water (solution 3). The solution 2 was then added dropwise to solution 1 under stirring followed by solution 3. Then, 2 mL hydrazinium hydroxide (7.49×10^{-4} mmol, 65 wt%) was added dropwise to the above solution. Finally, 0.05 mmol CTAB and 5.70×10^{-4} mmol PEG were added to the reaction solution under stirring for 5 min until the solution became homogeneous. The resulting homogeneous solution was sealed at 50 °C for 1 h (thermal method). Then the resulting precipitate was collected, filtered, and washed with ultrapure water and then with absolute ethanol for several times to remove any possible impurities and finally dried in *vacuum* before characterization.

The concentration of Zn was 43.70 Wt.% in the all of the Zn-based compounds which was determined using atomic absorption spectrometry (AAS). Preparation conditions for all compounds are summarized in Table 1.

2.3. Methods

2.3.1. Atomic absorption spectrometer (AAS)

The Zn^{+2} and co-metals (Mg^{+2}, Ca^{+2}, Al^{+3}, Ti^{+4}) contents were determined by Perkin Elmer Atomic Absorption Spectrometer 1100 model, United Kingdom, with a deuterium background corrector and zinc, magnesium, calcium, aluminum, and titanium hollow cathode lamps.

2.3.2. X-ray diffraction (XRD)

Crystalline nature of compounds were recorded by X'Pert PRO X-ray diffractometer, Philips Company, Netherlands, using CuK_α radiation (1.5405 Å) in the 2θ range of 20–80.

2.3.3. Scanning electron microscopy (SEM)

The external morphology of compounds was characterized by AIS 2100 microscope model with resolution 3.0 nm at 30 KeV, Seron Technologies INC, Korea. Samples were prepared by coating of solid particles into a conductive layer (gold).

2.3.4. Transmission electron microscopy (TEM)

The internal morphology of compounds was characterized by Philips-FEI 208S model, Philips Company, USA. Samples were prepared by dispersing solid product in ethanol by sonication. Few drops of the suspension were deposited on copper grids, which were then put into the desiccators for drying, followed by imaging.

Table 1
Experimental parameters for the preparation various formulations of the metal-doping Zn-based nanocomposites. See text for details.

No.	Compound code	[Zn(O)/M] formula	M[a]	[M] weight percent
1	**F1T**	[ZnO]	–	–
2	**F2T**	[Zn(O)/Mg]	Mg	4.9
3	**F3T**	[Zn(O)/Al]	Al	12.1
4	**F4T**	[Zn(O)/Ca]	Ca	15.0
5	**F5T**	[Zn(O)/Ti]	Ti	5.5

[a] M = Co-metal additive in zinc oxide compounds.

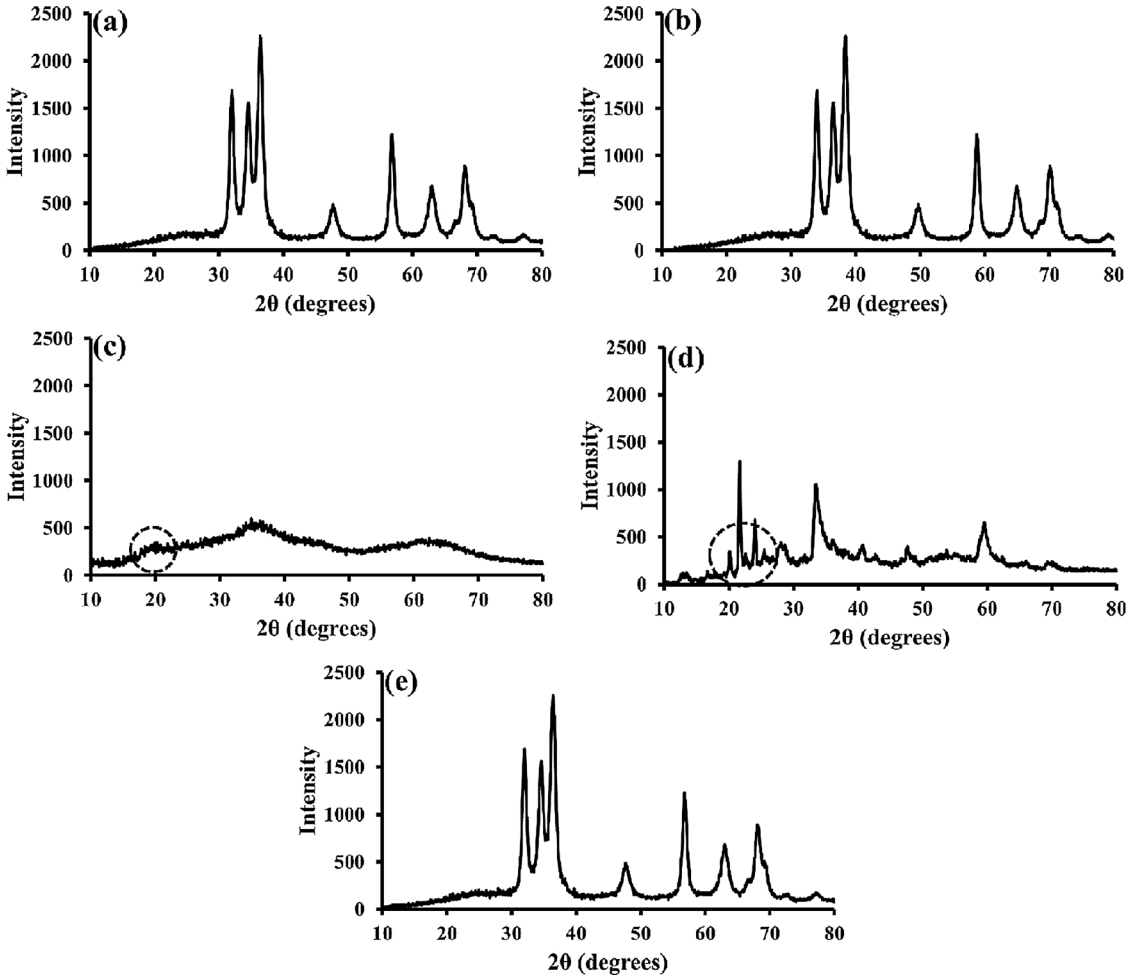

Fig. 1. XRD patterns of the (a) **F1T** ([ZnO]), (b) **F2T** ([Zn(O)/Mg]), (c) **F3T** ([Zn(O)/Al]), (d) **F4T** ([Zn(O)/Ca]), and (e) **F5T** ([Zn(O)/Ti]). The circles in (c) and (d) show aluminum oxide and calcium oxide, respectively.

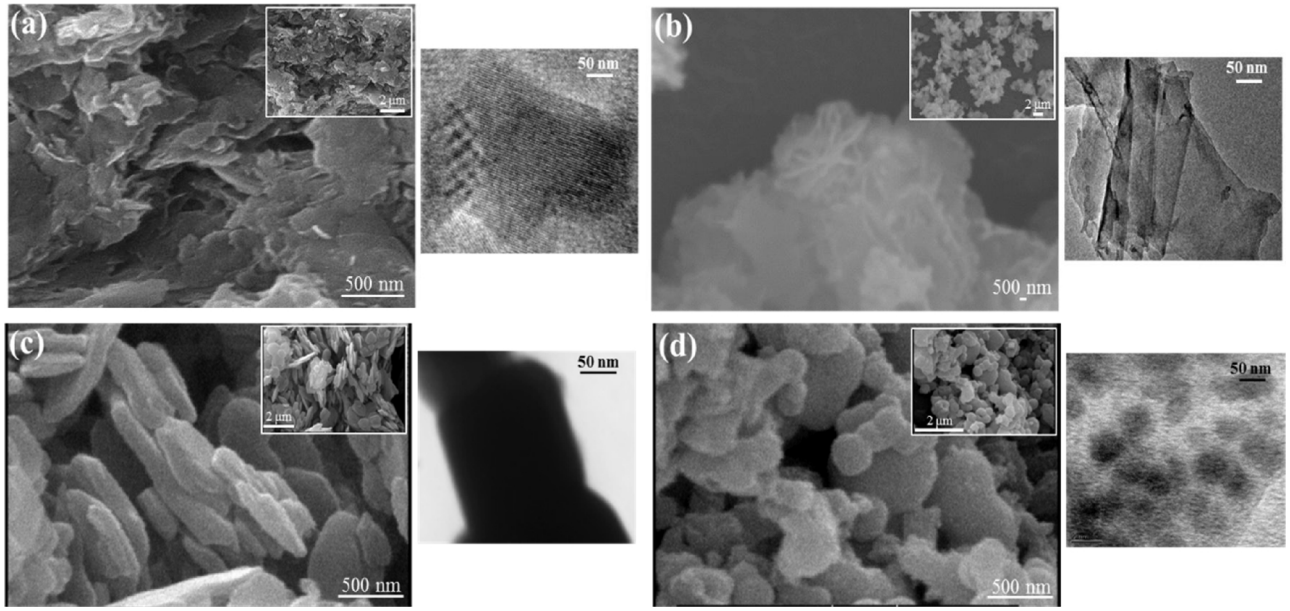

Fig. 2. SEM and TEM images of the (a) **F2T** ([Zn(O)/Mg]), (b) **F3T** ([Zn(O)/Al]), (c) **F4T** ([Zn(O)/Ca]), and (d) **F5T** ([Zn(O)/Ti]).

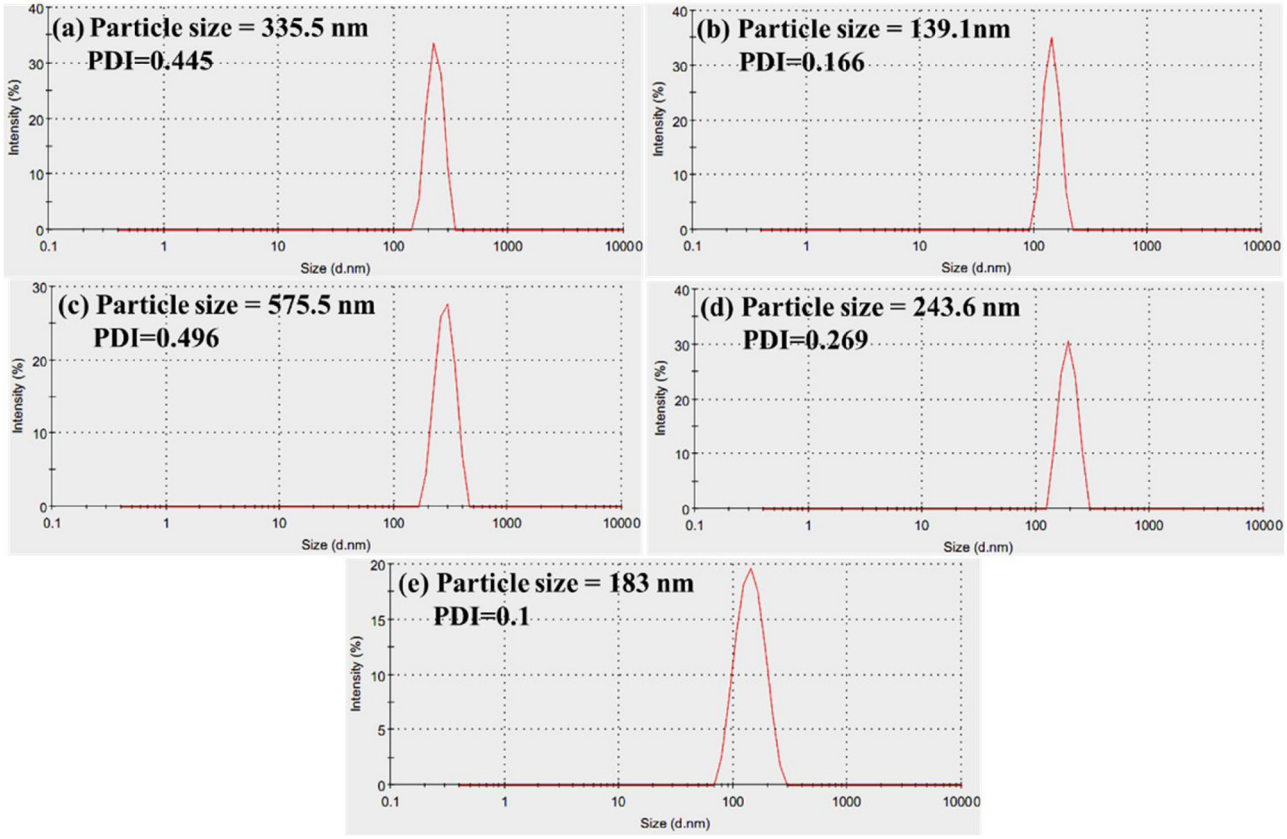

Fig. 3. Sample particle size distribution of the (a) **F1T** ([ZnO]), (b) **F2T** ([Zn(O)/Mg]), (c) **F3T** ([Zn(O)/Al]), (d) **F4T** ([Zn(O)/Ca]), (e) and **F5T** ([Zn(O)/Ti]) in culture medium.

Table 2
Particle size (nm) and PDI of various formulations of the Zn-based compounds in culture medium (mean ± SD, n = 3).

Sample	Formula	Particle size (nm)	PDI
F1T	[ZnO]	336 ± 2.7	0.5 ± 0.1
F2T	[Zn(O)/Mg]	138 ± 2.4	0.1 ± 0.0
F3T	[Zn(O)/Al]	575 ± 5.0	0.7 ± 0.2
F4T	[Zn(O)/Ca]	246 ± 8.0	0.3 ± 0.2
F5T	[Zn(O)/Ti]	185 ± 5.5	1.0 ± 0.0

2.3.5. Particle size analysis

Particle size has pronounced effects on the spectral properties of semiconductor materials [42]. The size distribution of compounds in culture medium was obtained using a Dynamic Light Scattering (DLS), Malvern, HPPS-5001 model equipped with a green laser at 532 nm, United Kingdom.

2.3.6. Fourier transformation infra-red (FT-IR) spectra

The surface properties of compounds were investigated by analysis of an ALPHA FT-IR spectrophotometer model of Bruker Company, Germany, at a spectral resolution of 4 cm^{-1} using KBr pellets in the range of 400–4000 cm^{-1} with a delicate beam condenser and a liquid nitrogen cooled MCT (mercury cadmium telluride)-Detector.

2.3.7. UV absorption properties

2.3.7.1. Diffuse reflectance spectroscopy (DRS). In order to calculate the precise value of optical band gaps (E_g, eV), as a measure of UV protection properties of semiconductors, UV–vis DRS analysis on compounds (powder) was employed here by Kubelka-Munk theory [43]. This analysis was recorded on Varian's Cary 100 UV–vis model spectrophotometer, USA.

2.3.7.2. UV–vis spectra. UV–vis spectra of 20 mg/L ZnO loading of **F1T**, **F2T**, **F3T**, **F4T**, **F5T**, and commercial ZnO in culture medium after 3 min sonication was recorded by CECIL Aurius Series CE 2021 UV/Vis Spectrophotometer, United Kingdom, using quartz cells of 1 cm optical path.

2.3.7.3. UV spectra for UV-blocking measurement. "Ultraviolet protection factor" (UPF) can be directly investigated using the ability of materials to block the UV radiation in the range of 280–400 nm [44]. The UV-blocking activity of 20 mg/L ZnO loading of **F1T**, **F2T**, **F3T**, **F4T**, **F5T**, and commercial ZnO was measured by a UV transmittance analyzer (CECIL Aurius Series CE 2021 UV/Vis Spectrophotometer) in culture medium, after 3 min sonication, using quartz cells of 1 cm optical path at room temperature.

2.4. Solubility measurement

The solubility of compounds in culture medium at 25 °C was studied in a beaker using samples of **F1T**, **F2T**, **F3T**, **F4T**, **F5T**, and commercial ZnO with 30 mg/L ZnO solid loading. Solutions (300 mL) were stirred for 24 h, while covered with aluminum foil to inhibit any photo-induced changes. Quantitative measurements were done at time intervals of 0.5, 6, 12, 18, and 24 h.

To separate solid particles from solution, solutions were passed through 0.2 µm filter. This was then followed by centrifugation at 12,000 rpm (3.15×10^4 rcf) for 60 min. Concentration of Zn^{+2} ions in supernatant was measured by AAS. The supernatants were also investigated under UV–vis light in the range of 200–700 nm to make sure that particulates are absent in the supernatant. No distinct peaks were observed, indicating that there is no particulate material in the supernatants after filtering and centrifugation. The pHs of the supernatants were also measured by a Metrohm 744 pH Meter.

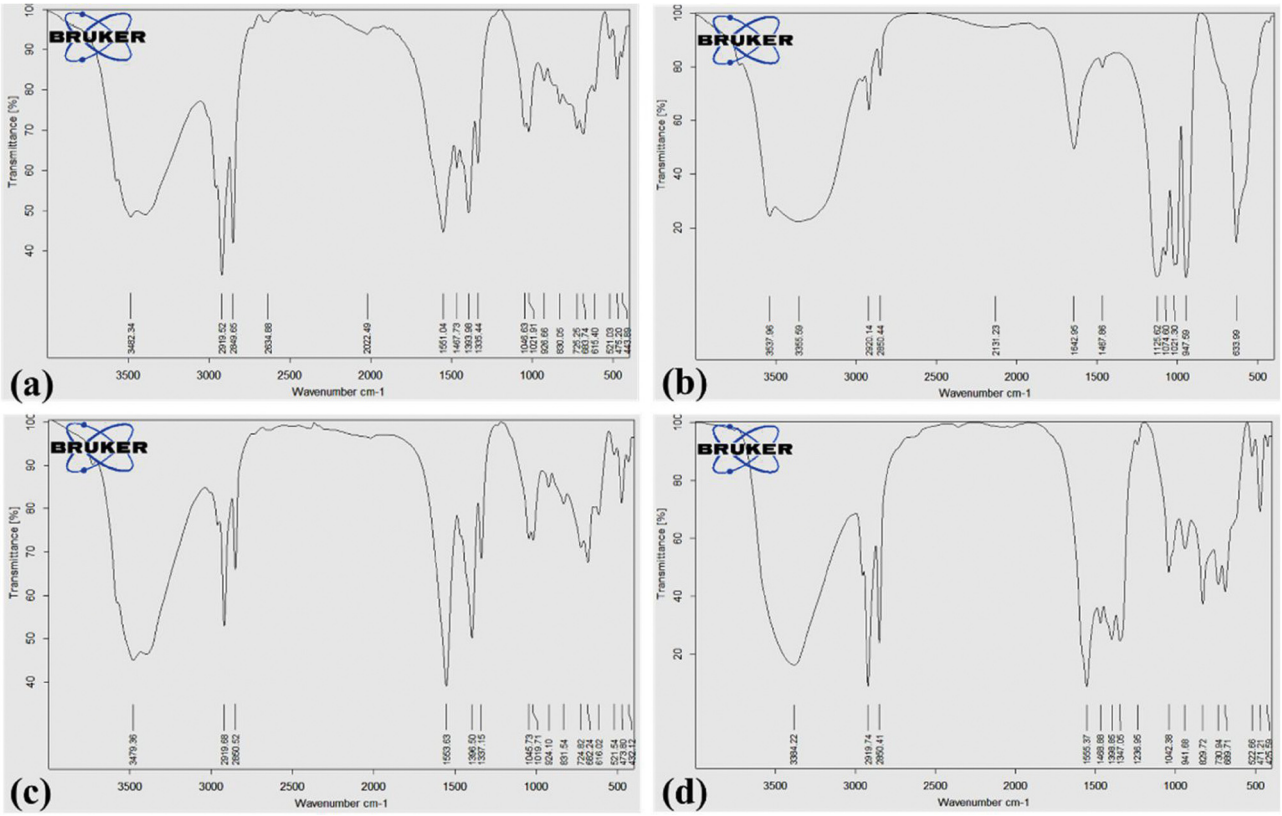

Fig. 4. FT-IR spectra of the (a) **F2T** ([Zn(O)/Mg]), (b) **F3T** ([Zn(O)/Al]), (c) **F4T** ([Zn(O)/Ca]), and (d) **F5T** ([Zn(O)/Ti]).

2.5. Release of Zn^{+2} ions from Zn-based compounds

Release of Zn^{+2} ions of **F1T**, **F2T**, **F3T**, **F4T**, **F5T**, and commercial ZnO with a ZnO solid loading of 20 mg/L in culture medium were carried out by dialysis method. Dialysis experiments were carried out in cellulose acetate dialysis tubing (12 KDa cutoff) filled with 3 mL nanoparticles dispersion and immersed in 100 fold of its volume of culture medium (300 mL) at 37 °C and covered with aluminum foil to inhibit any photo-induced dissolution. The dialysis was carried out under slow stirring (200 rpm) with a magnetic stirrer and the samples were drawn of receptor medium at time intervals of 0.5, 3, 6, 9, 12, 15, 18, 21, 24, and 48 h. The concentration of released Zn^{+2} was detected by AAS and the cumulative amount of the released Zn^{+2} was calculated and plotted against time.

2.6. Stability of nanoparticles in culture medium

2.6.1. Aggregation/particle size study

Understanding the stability of nanoparticles in liquid solution in terms of aggregation is very important. Particle size analysis is used as an indicator of nanoparticles stability. To evaluate this, particle sizes of **F1T**, **F2T**, **F3T**, **F4T**, and **F5T** suspensions in culture medium at room temperature were studied over time (1, 6, 12, 24, and 48 h).

2.6.2. Sedimentation and turbidity measurements

Based on colloidal theories on particle aggregation [45] and sedimentation [46], the dispersion stability of metallic nanoparticles can greatly influence on their bioavailability. The precipitation stability of the 20 mg/L ZnO loading of **F1T**, **F2T**, **F3T**, **F4T**, and **F5T** solutions in culture medium was measured using UV–vis spectrophotometer. The λ_{max} was measured at different times (during 48 h). The normalized absorbance A_i/A_0 (A_i = absorbance as a function of time, A_0 = initial absorbance) was calculated as a measure of sedimentation.

Turbidimetric test of 20 mg/L of ZnO loading of **F1T**, **F2T**, **F3T**, **F4T**, and **F5T** solutions in culture medium was also studied by 2100P-HACH Turbidimeter-USA (NTU-Normal Turbidity Unit) at room temperature over 48 h.

2.7. Cell culture studies

Cytotoxicity and protection effects of M-promoted ZnO nanocomposites (M = Mg, Ca, Al, Ti) were investigated using human skin (HFF-1) cells. Cells were seeded at a density of 4×10^4 cells per well of a 24-well plates [47] in complete culture medium (DMEM, 20% (v/v) heat-inactivated FBS, 10% (v/v) penicillin, and 100 IU ml^{-1} insulin). Cells were incubated for 24 h at 95/5% air/CO_2 incubator (ASTEC, BENCH-TOP Incubator EC-9, Japan) and 37 °C. Cells were exposed to Zn compounds and UV radiation for cytotoxicity and ROS measurement studies, as discussed below.

2.7.1. Exposure to Zn-based compounds

Cells were treated with 20 mg/L of **F1T**, **F2T**, **F3T**, **F4T**, and **F5T** for 24 h. Intracellular ROS production was then measured by ROS assay, as discussed later. The culture medium was also collected and centrifuged at 14,000 rpm (4.29×10^4 rcf). The concentration of released Zn^{2+} in all cellular supernatant was measured by AAS. The Zn^{2+} concentration in cells not exposed to nanocompounds suspension was served as a control.

2.7.2. UVA exposure

Exposing the skin cells to sunlight, especially to UVA radiation, leads to the photochemical generation of ROS [47,48]. It seems that Zn-based compounds can scavenge radiation-induced reactive oxygen (oxygen, hydroxyl, and superoxide radicals) intermediates in vitro [49,50]. To determine the protective effect of the Zn-based compounds (**F1T**, **F2T**, **F3T**, **F4T**, and **F5T**) in this research, Zn-treated cells were exposed to UVA radiation for 30 min at 2 W/cm^2 using UV lamp (mercury vapor lamp, with spectrum from 315 to 400 nm and

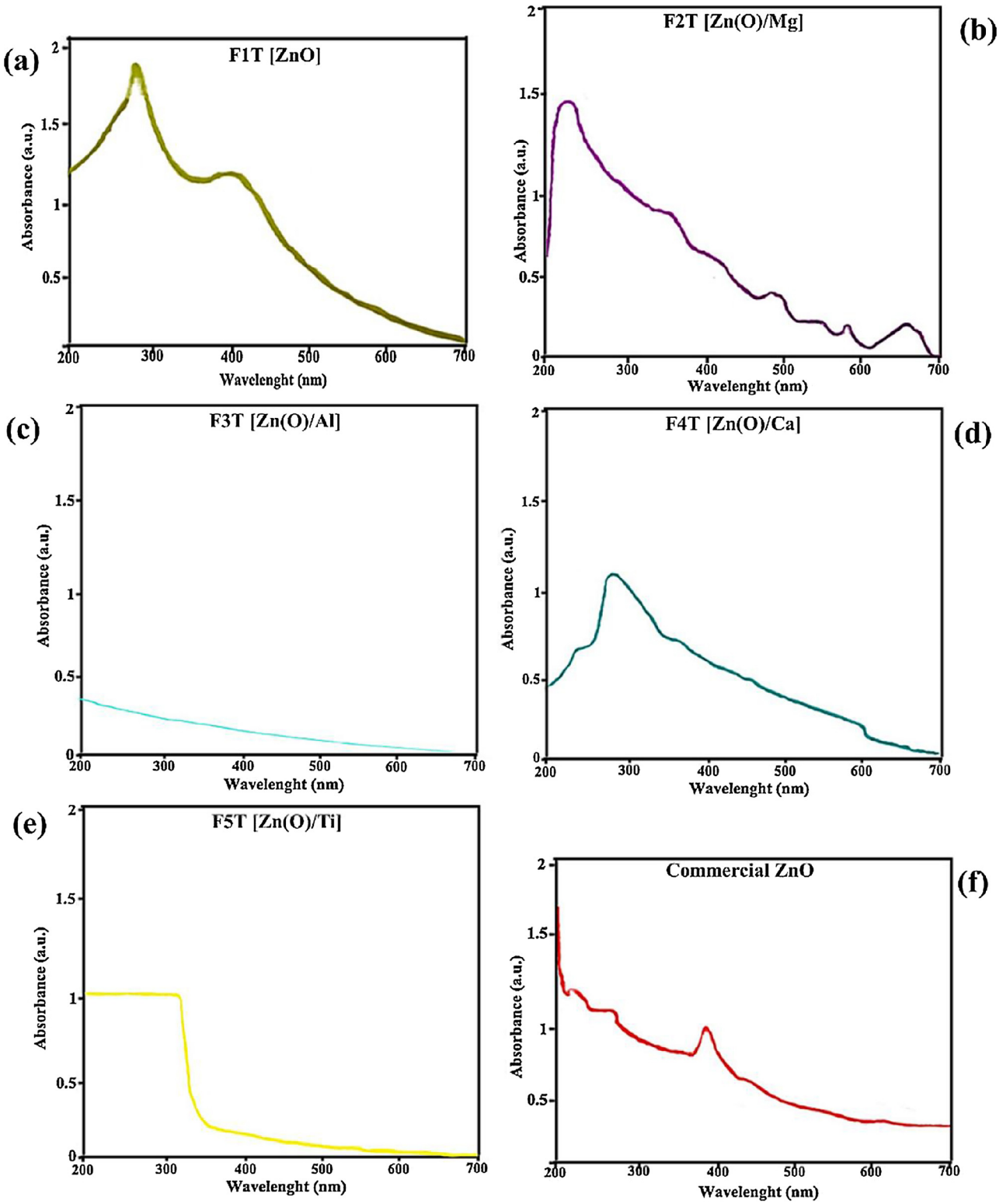

Fig. 5. Absorption spectra of **F1T**, **F2T**, **F3T**, **F4T**, **F5T**, and commercial ZnO in culture medium.

maximum intensity at 365 nm). The distance between cells and UV source was kept at 50 cm to prevent over heating during irradiation [50]. A compensated Kipp-Zonen thermopile coupled to a digital voltmeter was used to measure the UVA actual energy received by cells.

2.7.3. ROS measurement

High intracellular mitochondria ROS levels and oxidative assault have been cited as important factors for cytotoxicity-carcinogenesis of skin cells induced by UVA radiation and nanoscale metal oxides [51–53]. The generation of ROS by UVA radiation and Zn-based compounds (**F1T**, **F2T**, **F3T**, **F4T**, and **F5T**) in the HFF-1 cells was determined by a fluorometric assay using the intracellular oxidation of the molecular probe DCFH-DA [54].

Firstly, cells were treated with 20 mg/L **F1T**, **F2T**, **F3T**, **F4T**, and

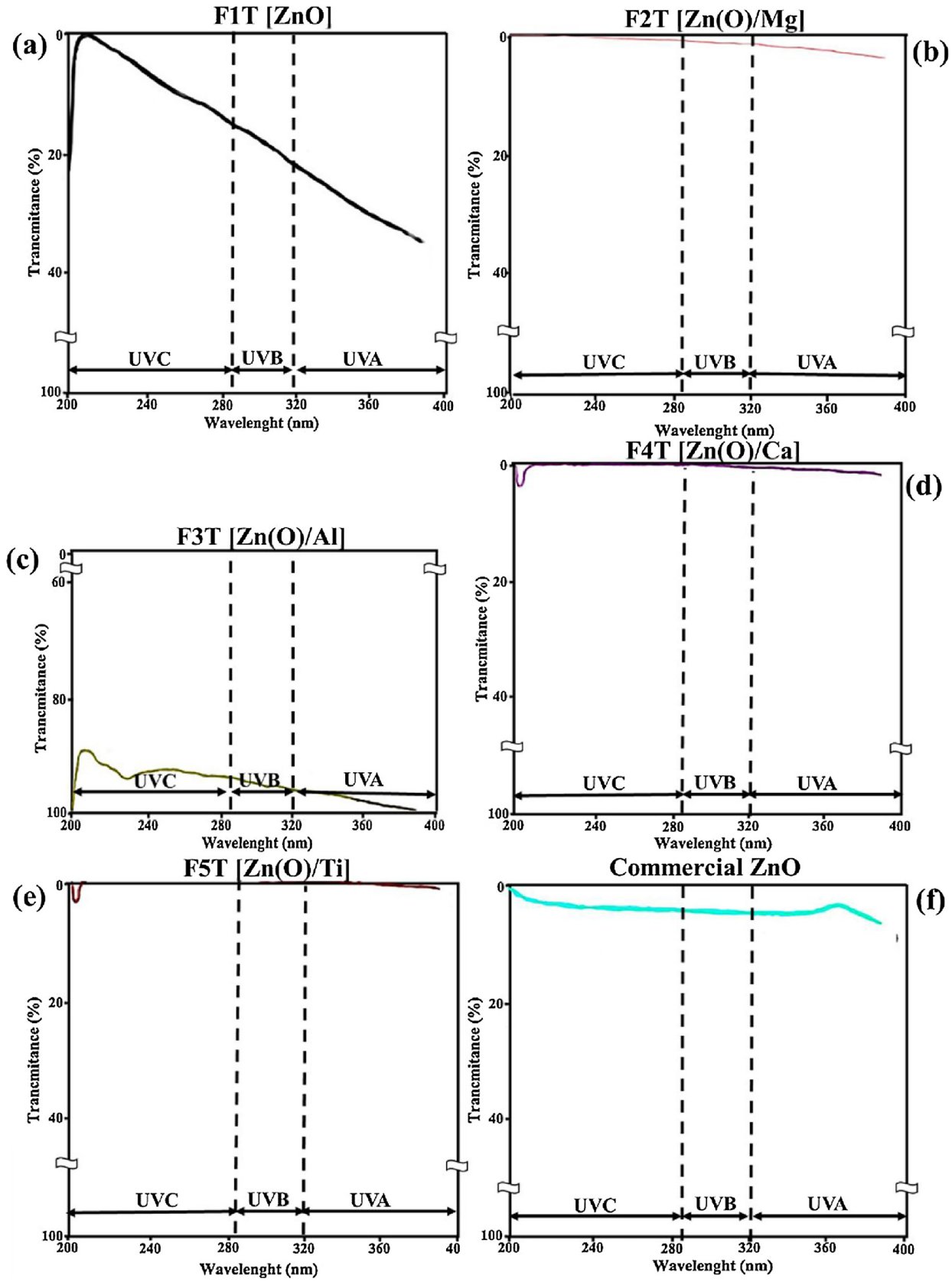

Fig. 6. Transmittance spectra of **F1T**, **F2T**, **F3T**, **F4T**, **F5T**, and commercial ZnO in culture medium.

Table 3
Optical band gap (E_g, eV) values of **F1T**, **F2T**, **F3T**, **F4T**, **F5T** and commercial ZnO.

Sample	Formula	E_g (eV)	Changes in comparison to ZnO
F1T (Control)	[ZnO]	3.07	0
F2T	[Zn(O)/Mg]	3.37	+0.30
F3T	[Zn(O)/Al]	2.75	−0.32
F4T	[Zn(O)/Ca]	3.37	+0.30
F5T	[Zn(O)/Ti]	3.6	+0.53
Commercial ZnO	ZnO	3.4	+0.33

F5T as described above. Cells were then washed with NS and PBS, and then incubated with 40 µM DCFH-DA for 30 min. At the end of incubation, supernatant containing the fluorescence of DCF, which is the oxidized product of DCFH, was measured with a fluorescence spectrophotometer (Infinite® 200 PRO, Tecan, Switzerland) using an excitation of 485 nm and an emission of 530 nm. The DCF concentration in cells not exposed to Zn-based compounds was used as control.

Secondary, Zn (**F1T**, **F2T**, **F3T**, **F4T**, and **F5T**)-treated cells were exposed to UVA radiation as described above. At the end of incubation, as described above, supernatant containing the fluorescence of DCF was measured with a fluorescence spectrophotometer. The DCF concentration in cells not exposed to Zn-based compounds and UVA radiation was used as control.

2.7.4. MTT assay

The cell viability after nanoparticles (**F1T**, **F2T**, **F3T**, **F4T**, and **F5T** with 20 mg/L) and UVA treatment was measured by MTT assay in the form of percentage relative death to an untreated control, without the Zn-based nanocompounds and UVA radiation. Measurements done by using ELISA microplate reader at 570 nm (BioTek, ELx808 Absorbance Microplate Reader, USA), as described by Alarifi and Ali [55].

2.8. Statistical analysis

Results were expressed as mean values and standard deviation (± SD) and the significance of the difference observed was analyzed by the Student's *t*-test. In all tests, a probability value of $P < 0.05$ was considered as statistically significant.

Also all the experiments were performed in triplicate and repeated three times to ensure reproducibility.

3. Results and discussion

3.1. Characterization the Zn-based compounds

3.1.1. Co-metal-content by AAS analyses

Atomic absorption studies showed that **F2T**, **F3T**, **F4T**, and **F5T** contained about 4.9, 12.1, 15.0, and 5.5 wt.% Ca^{+2}, Mg^{+2}, Al^{+3}, and Ti^{+4} ions respectively when 0.5 mmol chloride salt ($CaCl_2$, $MgCl_2{\cdot}6H_2O$, $AlCl_3$, $TiCl_4$) was used for synthesis (Table 1). Higher amount of chloride salt (0.75 mmol) did not change the M (co-metal)-content of the particles in considerable amount. The loading percent of Ca^{+2}, Mg^{+2}, Al^{+3}, and Ti^{+4} ions at this concentration (0.75 mmol) was found to be 5.1, 12.0, 15.9, and 5.0 wt.% in **F2T**, **F3T**, **F4T**,and **F5T**, respectively.

3.1.2. Crystalline and phase structure studies by XRD

Fig. 1 shows XRD patterns of **F1T**, **F2T**, **F3T**, **F4T**, and **F5T**. Zinc oxide showed a hexagonal structure with JCPDS card 36-1451. Bimetallic compounds also showed hexagonal structures, except for **F3T** that shows an amorphous structure. For all the bimetallic nanocomposites, shifts in the peaks angle of **F1T** XRD pattern (Fig. 1a) relative to ZnO were observed (Fig. 1b–e). The peak shifting may indicate the substitution of Zn^{+2} by M^{+n} (Mg^{+2}, Al^{+3}, Ca^{+2}, and Ti^{+4}) in hexagonal-ZnO crystal due to smaller ionic size of M^{+n} (Mg^{+2}, Al^{+3}, Ca^{+2}, and Ti^{+4}, 0.072, 0.053, 0.01, and 0.074 nm, respectively) compared to Zn^{+2} (0.074 nm). No diffraction peaks from co-metals species of Mg and Ti such as magnesium oxides and titanium oxides were detectable for **F2T** and **F5T** (Fig. 1b, e). For **F3T** and **F4T**, aluminum oxide and calcium oxide species were distinguishable (Fig. 1c, d).

3.1.3. Morphology, surface structure, and particle size analyses

Fig. 2 shows the typical SEM and TEM images of **F2T**, **F3T**, **F4T**, and **F5T**. As shown in Fig. 2, all nanocomposites (**F2T**, **F3T**, **F4T**, **F5T**) showed nano-metric size in the one dimensional (1-D) of their configuration (nanoflake morphology). Apparent nanoflakes of **F2T** and **F3T** had thinner diameters (about 25–50 nm, Fig. 2a, b) compared to **F4T** and **F5T** (about 50–100 nm, Fig. 2c, d). Also **F4T** and **F5T** exhibited monodisperse and homogeneous hexagonal configuration as angular forms (Fig. 2c, d).

Results of particle size analysis of **F2T**, **F3T**, **F4T**, and **F5T** are shown in Fig. 3 and Table 2. Particle size of ZnO (**F1T** without co-metal) is about 336 nm (Fig. 3a, Table 2). When Mg was added as co-metal, particle size was reduced by-about 2–4 times to about 140 nm (**F2T**, [Zn(O)/Mg], Fig. 3b, Table 2). **F4T** and **F5T** also provided smaller particle sizes (Fig. 3d, e, Table 2). But, Al-containing system (**F3T**) showed higher particle size than **F1T** (576 nm) (Fig. 3c, Table 2). The reason behind this phenomenon may be due to inhibition/acceleration of the growth rate of nucleations in the presence of co-metals during the synthesis process [19]. Polydispersity Index (PDI) of the synthesized Zn-based compounds shows uniformity in size (Fig. 3, Table 2).

Fig. 4 shows FT-IR spectra of **F2T**, **F3T**, **F4T**, and **F5T**. Peaks at 1330–1350, 1550–1570, and 2800–2900 cm^{-1} are attributed to PEG. Peaks at 1400–1500, 2800, and 2900 cm^{-1} are attributed to CTAB. These data show that PEG and CTAB are present on composites surface.

3.1.4. UV absorption properties

Figs. 5 and 6 show the absorbance and transmittance properties of **F1T**, **F2T**, **F3T**, **F4T**, **F5T**, and commercial ZnO solutions. All compounds exhibited high transparency in the visible region (400–700 nm, Fig. 5a–e). The UV absorbance properties in the bimetallic nanocomposites were improved significantly (except the **F3T**, [Zn(O)/Al], Figs. 5 and 6). It seems that the trapped UV light increased in 1-D structures which improved the optical path for the UV light absorption (morphology effect of compounds) [56,57]. According to anisotropic properties, crystalline materials with different morphologies and surfaces (different geometric and electronic structures) have different defect intensities [58] and active centers. These sites capture photo-induced electrons, recombination of photo-induced electrons and holes [59], and consequently different optical properties.

Table 4
Particle size (nm) of **F1T**, **F2T**, **F3T**, **F4T**, and **F5T** during 48 h in culture medium (mean ± SD, n = 3).

Sample	Zero time	1 h	6 h	12 h	24 h	48 h
F1T [ZnO]	475 ± 1.3	475 ± 4.4	475 ± 0.0	530 ± 1.5	535 ± 2.8	540 ± 2.3
F2T [Zn(O)/Mg]	178 ± 3.0	178 ± 1.5	179 ± 4.9	185 ± 3.0	181 ± 4.1	181 ± 5.0
F3T [Zn(O)/Al]	333 ± 4.1	345 ± 1.0	350 ± 6.2	400 ± 3.8	400 ± 4.5	400 ± 2.9
F4T [Zn(O)/Ca]	154 ± 3.2	179 ± 6.0	180 ± 3.0	178 ± 3.3	181 ± 1.5	180 ± 4.3
F5T [Zn(O)/Ti]	210 ± 1.5	223 ± 1.0	220 ± 2.4	225 ± 1.7	225 ± 1.5	225 ± 2.9

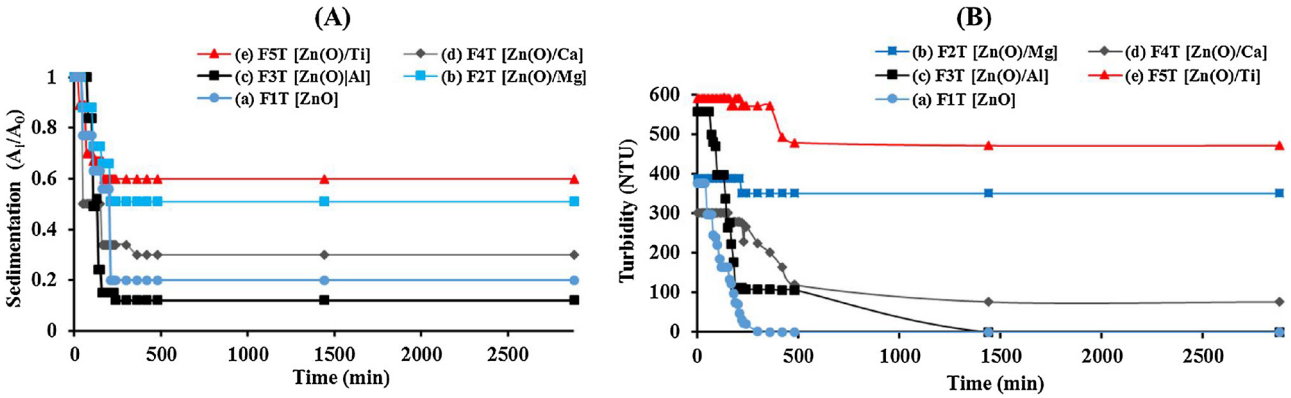

Fig. 7. (A) Sedimentation and (B) turbidimetric measurements of **F1T**, **F2T**, **F3T**, **F4T**, and **F5T** in culture medium and room temperature (mean ± SD, n = 3).

Table 5
$[Zn^{+2}]$ ions solubility and pH of saturated solutions of **F1T**, **F2T**, **F3T**, **F4T**, **F5T** and commercial ZnO in culture medium (mean ± SD, n = 3).

Sample	Formula	$[Zn^{+2}]$ (mg/L)	pH
Commercial ZnO	ZnO	11.2 ± 0.8	8.5
F1T	[ZnO]	8.9 ± 0.2	7.7
F2T	[Zn(O)/Mg]	2.7 ± 0.1	7.5
F3T	[Zn(O)/Al]	5.9 ± 0.4	7.6
F4T	[Zn(O)/Ca]	3.6 ± 0.2	7.7
F5T	[Zn(O)/Ti]	0.1 ± 0.0	7.3

In order to determine the precise value of energy band gap (E_g) of **F1T**, **F2T**, **F3T**, **F4T**, **F5T**, and commercial ZnO, we used optical absorption method on UV–vis diffuse reflectance by Kubelka-Munk theory [43] (Table 3). Band gap of ZnO in **F1T** is selected as control value (3.07 eV). It is clear that the absorption index metal-doped ZnO samples are showed the red-shifted (**F3T**) and blue-shifted (**F2T**, **F4T**, and **F5T**) in the band gap energy compared to undoped ZnO sample. These shifts in metal-doped ZnO samples are attributed to exchange interaction between the band electrons (ZnO) and the electrons of valance orbitals of the metal ion (metals doping) substituting cation [60]. This interaction result is moving of valance band and conductive band of metal-doped ZnO samples (Table 3). Also according to results of absorption and transmittance spectra, the unprecedented magnitude of both spectra (Figs. 5 and 6) for metal-doped ZnO samples may be due to creation of new, accessible, and localize electronic states in the band gap of them that are known to induce UV–vis-light absorption and transmittance. This phenomenon is expected to increase UV-carrier concentrations which lead to the Burstein-Moss effect [61]. Also special particle size (Fig. 3, Table 3) and morphology (Fig. 2) of metal-doped ZnO samples might affect band gap and electronic sites due to quantum confinement effects of metals particles in these properties.

3.2. Time-dependent stability tests of Zn-based compounds

3.2.1. Aggregation measurement

Particle size of **F1T**, **F2T**, **F3T**, **F4T**, and **F5T** suspensions in culture medium and room temperature was showed in Table 4. It can be said that particle sizes of **F2T**, **F4T**, and **F5T** suspensions are stable over 48 h. However particle sizes of **F1T** and **F3T** increased about 65 and 67 nm during 48 h possibly due to agglomeration in culture medium.

3.2.2. Sedimentation and turbidity measurements

Fig. 7A, B shows the time-dependent sedimentation and turbidity rates of **F1T**, **F2T**, **F3T**, **F4T**, and **F5T** suspensions in culture medium during 48 h. The initial sedimentation rate of all Zn-based compounds is very fast nearly till 2 h (Fig. 7A). The **F2T** and **F5T** suspensions (Fig. 7Ab, e) are more stable compared to **F1T**, **F3T**, and **F4T** suspensions (Fig. 7Aa, c, d) over 48 h.

The initial turbidity of **F3T** and **F5T** suspensions (Fig. 7Bc, e) is more compared to **F1T**, **F2T**, and **F4T** suspensions (Fig. 7Ba,b,d). Turbidity value of **F1T** and **F3T** suspensions was zero after 48 h (Fig. 7Ba, c).

3.3. Solubility of Zn-based compounds in culture medium

Table 5 shows the solubility and pH of **F1T**, **F2T**, **F3T**, **F4T**, **F5T**, and commercial ZnO in culture medium at room temperature after equilibrium.

Solubility of prepared ZnO (**F1T**, 8.9 mg/L) is close to commercial ZnO (11.2 mg/L, Table 5). There is a decrease in solubility for all metal-

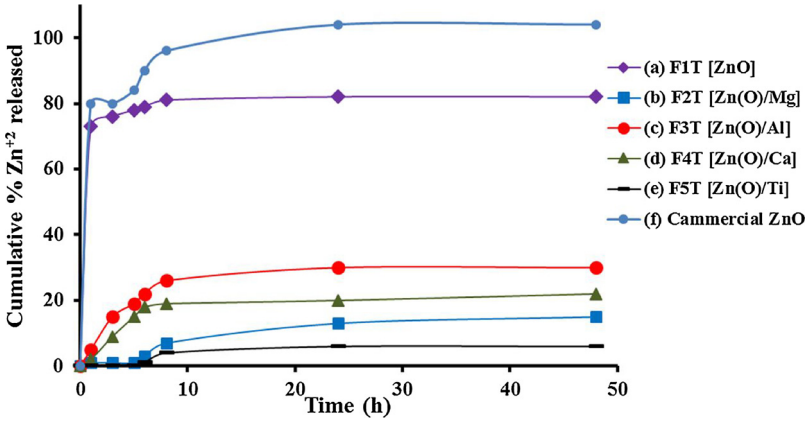

Fig. 8. Cumulative released Zn^{+2} profiles of **F1T**, **F2T**, **F3T**, **F4T**, **F5T**, and commercial ZnO in culture medium and 37 °C for 48 h (mean ± SD, n = 3).

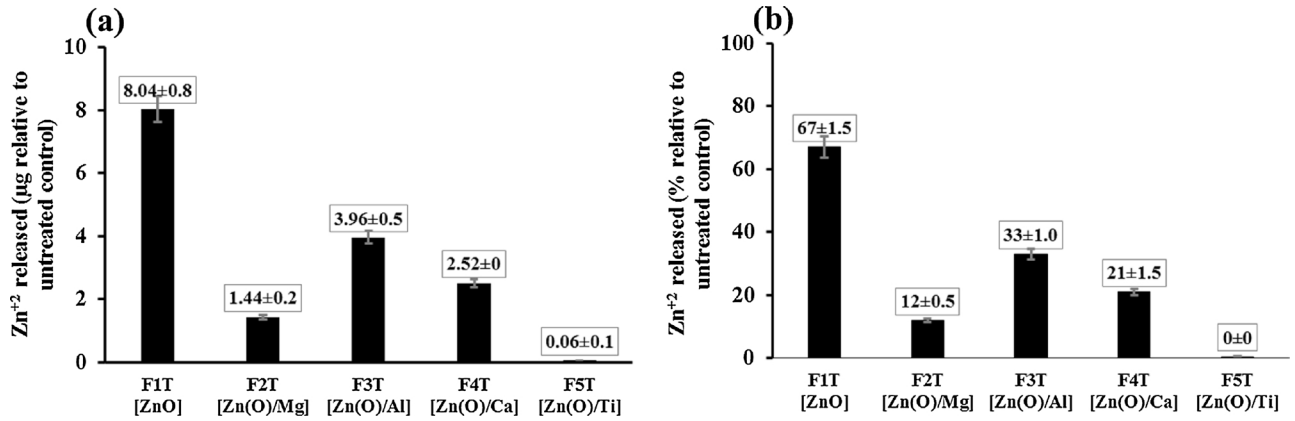

Fig. 9. Zn^{+2} release from **F1T**, **F2T**, **F3T**, **F4T**, and **F5T** in the presence of HFF-1 cell over 24 h (a) pure amount and (b) percent (mean ± SD, n = 3).

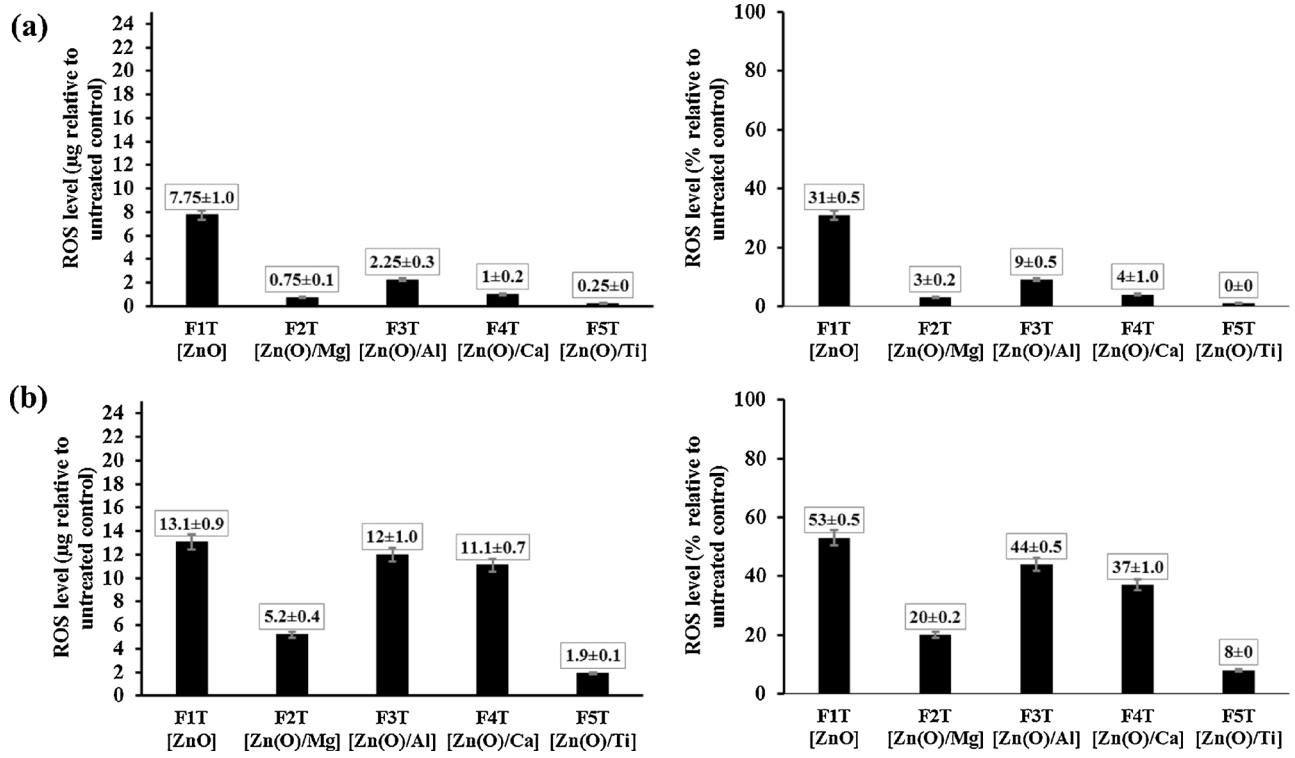

Fig. 10. Nature-dependent measurements of intracellular ROS production (pure amount and percent) in HFF-1 cells (a) for cells exposed to Zn-based compounds (in compared to untreated control) and (b) for cells exposed to Zn-based compounds and UVA radiation (in compared to untreated control) (mean ± SD, n = 3).

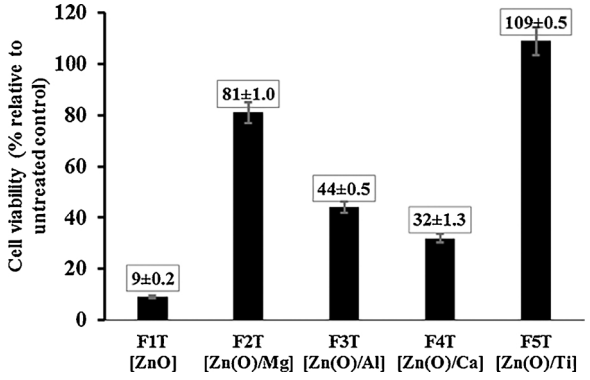

Fig. 11. Nature-dependent cell viability of HFF-1 cells exposed to Zn-based compounds and UVA radiation (mean ± SD, n = 3).

doping ZnO nanocomposites (**F2T**, **F3T**, **F4T**, **F5T**) compared to undoped ZnO (**F1T**). This phenomenon may be due to change in crystalline lattice and structural strength of the metal–oxide bond (vacancies, interstitial elements, degree of ordering, and etc., Figs. 1–6, Tables 2 and 3) of metal-doping Zn-based nanocomposites [9,62]. Also among metal-doping Zn-based nanocomposites, **F5T** shows lower solubility (0.1 mg/L) compared to **F2T**, **F3T**, and **F4T** (2.7–5.9 mg/L). The pH of suspensions was in the range of 7.3–7.7 (Table 5).

3.4. Release of Zn^{+2} ions from the Zn-based nanocompounds in culture medium

The observed cytotoxicity of ZnO nanoparticles has been attributed to dissolve Zn^{+2} of their network in environment [63]. In vitro toxic concentrations of Zn^{+2} typically exceed 10 mg/L [64]. Fig. 8 shows cumulative released Zn^{+2} profiles of **F1T**, **F2T**, **F3T**, **F4T**, **F5T**, and commercial ZnO in culture medium at 37 °C during 48 h. For commercial ZnO, Zn^{+2} ions released completely (Fig. 8f). For undoped ZnO

compound, Zn^{+2} ions released about 80% and reached to steady state after about 5 h (**F1T**, Fig. 8a).

Metal-doping ZnO nanocomposites showed Zn^{+2} ions release of lower than 30% (**F2T**, **F3T**, **F4T**, **F5T**, Fig. 8b–e). **F3T** and **F4T** showed a burst release followed by a steady state after about 8 h and 30 and 22% of Zn^{+2} ions released after 48 h, respectively (Fig. 8c, d). **F2T** and **F5T** were found stable with lowest release. **F5T** showed very lower release of about 6% and **F2T** only about 15%, (Fig. 8b, e) after 6 h.

Also the release medium of **F2T**, **F3T**, and **F4T** was seen to contain about 3, 76, and 44% of Mg^{+2}, Al^{+3}, and Ca^{+2} ions released, respectively, but for **F5T**, no Ti^{+4} was detected in the release medium.

3.5. Release of Zn^{+2} ions from nanocompounds in the presence of HFF-1 cells

Amount of released Zn^{+2} ions in the presence of cells was 12, 33, 21, and 0% after exposure to 20 mg/L of **F2T**, **F3T**, **F4T**, and **F5T** solutions, respectively (Fig. 9). Results showed that the nature of ZnO structure affects the amount of released Zn^{+2} ions in the presence of HFF-1 cells.

Also 67% Zn^{+2} ions released after exposure to 20 mg/L of **F1T** (undoped ZnO compound, Fig. 9). According to above results, stability of metal-doped ZnO nanocomposites (**F2T**, **F3T**, **F4T**, **F5T**) has increased compared to undoped ZnO (**F1T**). The metal dopant (Mg^{+2}, Al^{+3}, Ca^{+2}, Ti^{+4}), similar to useful metallic chelator at crystalline structure of ZnO, avoid released Zn^{+2} ions of ZnO network into culture medium.

No co-metal ions (Mg^{+2}, Al^{+3}, Ca^{+2}, Ti^{+4}) were detected for all metal-doping Zn-based nanocomposites (**F2T**, **F3T**, **F4T**, **F5T**) in the cellular medium in the presence of HFF-1 cells.

For **F2T**, **F3T**, **F4T**, the percent of released Zn^{+2} ions in the presence of HFF-1 cells (Fig. 9) was similar to cell-free conditions (Fig. 8b–d). However, **F5T** did not show any released Zn^{+2} ions in the presence of HFF-1 cells (Fig. 9), opposite to plain culture medium that showed a 6% release (Fig. 8e).

3.6. Intracellular ROS production

The ROS production percentages in Zn-treated cells relative to untreated ones were 31, 3, 9, 4, 0% for **F1T**, **F2T**, **F3T**, **F4T**, **F5T**, respectively (Fig. 10a). These results showed that doped compounds have lower effect on formation of intracellular ROS compared to **F1T**. This phenomenon may be due to high stability of ZnO particles in the presence of co-metal.

When the cells were treated with UVA radiation in the presence of Zn-based compounds, 52, 20, 44, 37, 8% ROS were formed for **F1T**, **F2T**, **F3T**, **F4T**, **F5T**, respectively (Fig. 10b). It seems that photo-catalytic protection of ZnO after incorporation of co-metal in its network was increased due to change in the local crystal lattice environment (strength bond, vacancies, degree of ordering of elements, and etc.) of metal ions guest in ZnO host. However, among these compounds, **F5T** acts as a strong preservative and **F2T**, **F3T**, **F4T** act as a relatively lower preservative against UVA radiation.

Fig. 10a, b also shows that the effects of UVA radiation on intracellular ROS generation are more than that of Zn-based compounds.

3.7. Cell viability study

Nature-dependent protective effect of Zn-based compounds in HFF-1 cells after exposure to UVA radiation was demonstrated by MTT assay (Fig. 11). Cells showed a viability of about 9% when was treated with **F1T** (ZnO). For **F2T** and **F5T**, cell viability was increased sharply to 81 and 109%, respectively. Others Zn-based compounds also showed higher viabilities than ZnO, 44 and 32% for **F3T**, and **F4T** respectively. Among metal-doped ZnO nanocomposites, the lower protective effects of **F3T** and **F4T** compared to **F2T** and **F5T** were attributed to interaction aluminum oxide and calcium oxide on ZnO surface in **F3T** and **F4T**, respectively (Fig. 1c, d).

This phenomenon might be discussed by band-gap energy as discussed below. As according to DRS results (Table 3), due to interaction between the band electrons of ZnO and the electrons of valance orbitals of co-metal (Ca^{+2}, Mg^{+2}, Al^{+3}, Ti^{+4}), new defects were appeared in band gap of ZnO. Therefore band gap position of composites was changed and new storage energy source was formed. It seems that the new electronic states (E_g) in the metal-doped ZnO composites are greatly responsible for special absorbance/transmittance property (photo-catalyst activity) of these composites. Therefore these composites act as a protective agents for cells against UVA radiation.

4. Conclusion

In summary, different ZnO nanocomposites containing Mg^{+2}, Al^{+3}, Ca^{+2}, and Ti^{+4} (as co-metals) were synthesized and characterized here. Dopant ions were uniformly incorporated and replaced zinc sites in the hexagonal crystal lattice. These newly developed nanocomposites were able to protect of human skin cells (HFF-1) against UVA radiation photodamage. The protection was more than plain ZnO and the cytotoxicity of the doped nanocompounds was lower than non-doped ZnO.

This study is an initial attempt toward synthesis of the bimetallic zinc nanostructures. Modification of synthetic approach, purity of chemical of nanocomposites, and application of these compounds in a wide range of human skin protection, including preparation of a safer nano-zinc sunscreen are in progress in our laboratories.

Acknowledgments

This work was financially supported by School of Pharmacy, Shahid Beheshti University of Medical Sciences, Tehran, Iran and a sabbatical grant to Parvaneh Ghaderi-Shekhi Abadi from Razi University, Kermanshah, Iran.

References

[1] A. Svobodova, D. Walterova, J. Vostalova, Ultraviolet light induced alteration to the skin, Biomed. Pap. Med. Fac. Univ. Palacky Olomouc Czech Repub. 150 (1) (2006) 25–38.
[2] C. Kielbassa, L. Roza, B. Epe, Wavelength dependence of oxidative DNA damage induced by UV and visible light, Carcinogenesis 18 (1997) 811–816.
[3] A. Stary, C. Robert, A. Sarasin, Deleterious effects of ultraviolet A radiation in human cells, Mutat. Res. 383 (1997) 1–8.
[4] J.M. Laat, F.R. Gruijl, The role of UVA in the aetiology of non-melanoma skin cancer, Cancer Surv. 26 (1996) 173–191.
[5] R.B. Harris, D.S. Alberts, Strategies for skin cancer prevention, Int. J. Dermatol. 43 (2004) 243–251.
[6] M.J. Osmond, M.J. Mccall, Zinc oxide nanoparticles in modern sunscreens: an analysis of potential exposure and hazard, Nanotoxicology (2010) 15–41.
[7] J.A. Ruszkiewicz, A. Pinkas, B. Ferrer, T.V. Peres, A. Tsatsakis, M. Aschner, Neurotoxic effect of active ingredients in sunscreen products, Toxicol. Rep. 4 (2017), http://dx.doi.org/10.1016/j.toxrep.2017.05.006.
[8] P. Borm, F.C. Klaessig, T.D. Landry, B. Moudgil, J. Pauluhn, K. Thomas, R. Trottier, S. Wood, Research strategies for safety evaluation of nanomaterials, part V: role of dissolution in biological fate and effects of nanoscale particles, Toxicol. Sci. 90 (1) (2006) 23–32.
[9] S. George, S. Pokhrel, T. Xia, B. Gilbert, Z.X. Ji, M. Schowalter, A. Rosenauer, R. Damoiseaux, K.A. Bradley, L. Mädler, A.E. Nel, Use of a rapid cytotoxicity screening approach to engineer a safer zinc oxide nanoparticle through iron doping, ACS Nano 4 (1) (2010) 15–29.
[10] T. Xia, M. Kovochich, M. Liong, L. Madler, B. Gilbert, H. Shi, J.I. Yeh, J.I. Zink, A.E. Nel, Comparison of the mechanism of toxicity of zinc oxide and cerium oxide nanoparticles based on dissolution and oxidative stress properties, ACS Nano 2 (2008) 2121–2134.
[11] M. Mortimer, K. Kasemets, A. Kahru, Toxicity of ZnO and CuO nanoparticles to ciliated protozoa Tetrahymena thermophile, Toxicology 269 (2010) 182–189.
[12] J.P. Jolivet, C. Froidefond, A. Pottier, C. Chaneac, S. Cassaignon, E. Tronc, P. Euzen, Size tailoring of oxide nanoparticles by precipitation in aqueous medium: a semi-quantitative modeling, J. Mater. Chem. 14 (2004) 3281–3288.
[13] M. Farré, K. Gajda-Schrantz, L. Kantiani, D. Barcelo, Ecotoxicity and analysis of nanomaterials in the aquatic environment, Anal. Bioanal. Chem. 393 (2009) 81–95.
[14] T.J. Brunner, P. Wick, P. Manser, P. Spohn, R.N. Grass, L.K. Limbach, A. Bruinink, W.J. Stark, In vitro cytotoxicity of oxide nanoparticles: comparison to asbestos,

silica, and the effect of particle solubility, Environ. Sci. Technol. 40 (2006) 4374–4381.
[15] C.M. Sayes, A.M. Gobin, K.D. Ausman, J. Mendez, J.L. West, V.L. Colvin, Nano-C_{60} cytotoxicity is due to lipid peroxidation, Biomaterials 26 (2005) 7587–7595.
[16] T.C. Long, N. Saleh, R.D. Tilton, G.V. Lowry, B. Veronesi, Titanium dioxide (P25) produces reactive oxygen species in immortalized brain microglia (BV2): implications for nano-particle neurotoxicity, Environ. Sci. Technol. 40 (2006) 4346–4352.
[17] A. Khayatiana, V. Asgaria, A. Ramazania, S.F. Akhtarianfarb, M. Almasi Kashia, S. Safa, Diameter-controlled synthesis of ZnO nanorods on Fe-doped ZnO seed layer and enhanced photodetection performance, Mater. Res. Bull. 94 (2017) 77–88.
[18] M. Pal, S. Bera, S. Sarkar, S. Jana, Influence of Al doping on microstructural, optical and photocatalytic properties of sol-gel based nanostructured zinc oxide films on glass, RSC Adv. 4 (2014) 11552–11563.
[19] Y.P. Du, Y.W. Zhang, L.D. Sun, C.H. Yan, Efficient energy transfer in monodisperse Eu-doped ZnO nanocrystals synthesized from metal acetylacetonates in high-boiling solvents, J. Phys. Chem. C 112 (32) (2008) 12234–12241.
[20] P. Ghaderi-Shekhi Abadi, E. Rafiee, Sh. Nadri, G. Hajian, M. Joshaghani, Synthesis and activity evaluation of a $FeCl_2$-promoted palladium hollow nano-sphere heterogeneous catalyst in Mizoroki-Heck coupling reactions, Appl. Catal. A Gen. 487 (2014) 139–147.
[21] P. Ghaderi-Shekhi Abadi, E. Rafiee, M. Joshaghani, Pd-PVP-Fe (palladium-poly(N-vinylpyrrolidone)-iron) catalyzed S-arylation of thiols with aryl halides in aqueous media, Inorg. Chim. Acta 451 (2016) 162–170.
[22] E. Rafiee, M. Joshaghani, P. Ghaderi-Shekhi Abadi, Effect of a weak magnetic field on the Mizoroki-Heck coupling reaction in the presence of wicker-like palladium-poly(N-vinylpyrrolidone)-iron nanocatalyst, J. Magn. Magn. Mater. 408 (2016) 107–115.
[23] M. Ashfaq, N. Verma, S. Khan, Copper/zinc bimetal nanoparticles-dispersed carbon nanofibers: a novel potential antibiotic material, Mater. Sci. Eng. C Mater. Biol. Appl. 59 (2016) 938–947.
[24] J. Xiao, A. Kuc, T. Frauenheim, T. Heine, Stabilization mechanism of ZnO nanoparticles by Fe doping, Phys. Rev. Lett. 112 (2014) 106102-1-106102-5.
[25] Y. Okazakia, E. Gotoh, Comparison of metal release from various metallic biomaterials in vitro, Biomaterials 26 (2005) 11–21.
[26] G. Nagaraju Udayabhanu Shivaraj, S.A. Prashanth, M. Shastri, K.V. Yathish, C. Anupama, D. Rangappa, Electrochemical heavy metal detection, photocatalytic, photoluminescence, biodiesel production and antibacterial activities of Ag-ZnO nanomaterial, Mater. Res. Bull. 94 (2017) 54–63.
[27] S. Jana, A.S. Vuk, A. Mallick, B. Orel, P.K. Biswas, Effect of boron doping on optical properties of sol-gel based nanostructured zinc oxide films on glass, Mater. Res. Bull. 46 (2011) 2392–2397.
[28] P. Pradhan, J.C. Alonso, M. Bizarro, Photocatalytic performance of ZnO: Al films under different light sources, Int. J. Photoenergy 2012 (2012) 780462–780469.
[29] Q. Zhang, T. Gao, J.M. Andino, Y. Li, Copper and iodine co-modified TiO_2 nanoparticles for improved activity of CO_2 photoreduction with water vapor, Appl. Catal. B Environ. 123–124 (2012) 257–264.
[30] D.E. Coricovac, E.A. Moacă, I. Pinzaru, C. Cîtu, C. Soica, C.V. Mihali, C. Păcurariu, V.A. Tutelyan, A. Tsatsakis, C.A. Dehelean, Biocompatible colloidal suspensions based on magnetic iron oxide nanoparticles: synthesis, characterization and toxicological profile, Front. Pharmacol. 8 (2017) 1–18.
[31] M. Ni, M.K.H. Leung, D.Y.C. Leung, K. Sumathy, A review and recent developments in photocatalytic water-splitting using TiO_2 for hydrogen production, Renew. Sustain. Energy Rev. 11 (2007) 401–425.
[32] S. Manivannan, R. Ramaraj, Core-shell Au/Ag nanoparticles embedded in silicate sol-gel network for sensor application towards hydrogen peroxide, J. Chem. Sci. 121 (2009) 735–743.
[33] G.A. Petkova, K. Záruba, P. Žvátora, V. Král, Gold and silver nanoparticles for biomolecule immobilization and enzymatic catalysis, Nanoscale Res. Lett. 7 (2012) 287–296.
[34] J. Arikrishnan, S.K.T. Sheerin, M. Murugavelu, B. Karthikeyan, Experimental and theoretical studies on sensing adenine by Ag, Au and Ag-Au bimetallic nanoparticles, Indian J. Chem. 50 (2011) 46–50.
[35] W. Liu, F. Xiu, K. Sun, Y.H. Xie, K.L. Wang, Y. Wang, J. Zou, Z. Yang, J. Liu, Na-doped p-type ZnO microwires, J. Am. Chem. Soc. 132 (8) (2010) 2498–2499.
[36] C.B. Tay, S.J. Chua, K.P. Loh, Stable p-type doping of ZnO film in aqueous solution at low temperatures, J. Phys. Chem. C 114 (21) (2010) 9981–9987.
[37] Y.J. Zeng, Z.Z. Ye, W.Z. Xu, D.Y. Li, J.G. Lu, L.P. Zhu, B.H. Zhao, Dopant source choice for formation of p-type ZnO: Li acceptor, Appl. Phys. Lett. 88 (2006) 062107.
[38] S. Cho, Properties of nitrogen and aluminium-co-doped ZnO thin films grown with different nitrogen flow ratios for solar cell applications, Curr. Appl. Phys. 10 (2010) S443–S446.
[39] R. Qin, J. Zheng, J. Lu, L. Wang, L. Lai, G. Luo, J. Zhou, H. Li, Z. Gao, G. Li, W.N. Mei, Origin of p-type doping in zinc oxide nanowires induced by phosphorus doping: a first principles study, J. Phys. Chem. C 113 (22) (2009) 9541–9545.
[40] S.P. Wang, C.X. Shan, B.H. Li, J.Y. Zhang, B. Yao, D.Z. Shen, X.W. Fan, A facile route to arsenic-doped p-type ZnO films, J. Cryst. Growth 311 (2009) 3577–3580.
[41] X.H. Pan, W. Guo, Z.Z. Ye, B. Liu, Y. Che, H.P. He, X.Q. Pan, Optical properties of antimony-doped p-type ZnO films fabricated by pulsed laser deposition, J. Appl. Phys. 105 (2009) 113516.
[42] N. Serpone, D. Lawless, R. Khairutdinov, Size effects on the photophysical properties of colloidal anatase TiO_2 particles: size quantization or direct transitions in this indirect semiconductor? J. Phys. Chem. 99 (1995) 16646–16654.
[43] T. Ates, C. Tatar, F. Yakuphanoglu, Preparation of semiconductor ZnO powders by sol-gel method: humidity sensors, Sens. Actuators A Phys. 190 (2013) 153–160.
[44] M. Shateri-Khalilabad, M.E. Yazdanshenas, Bi-functionalization of cotton textiles by ZnO nanostructures: antimicrobial activity and ultraviolet protection, Text. Res. J. 83 (10) (2013) 993–1004.
[45] M.V. Smoluchowski, Versuch einer mathematischen Theorie der Koagulationskinetik kolloider Lösungen, Zeltschrinf. physllc. Chem. XCI 92 (1917) 129–168.
[46] G.G. Stokes, On the effect of the internal friction of fluids on the motion of pendulums, Trans. Camb. Philos. Soc. IX 8 (1850).
[47] A.O. Oyewole, M.C. Wilmot, M. Fowler, M.A. Birch-Machin, Comparing the effects of mitochondrial targeted and localized antioxidants with cellular antioxidants in human skin cells exposed to UVA and hydrogen peroxide, FASEB J. 28 (2014) 485–494.
[48] H. Yin, P.S. Casey, Effects of surface chemistry on cytotoxicity, genotoxicity, and the generation of reactive oxygen species induced by ZnO nanoparticles, Langmuir 26 (19) (2010) 15399–15408.
[49] E.J. Dudek, J.G. Peak, R.M. Roth, M.J. Peak, Protection Against UVA-Induced Photo-Oxidative Damage in Mammalian Cell Lines Expressing Increased Levels of Metallothionein, (1990) ANL/CP–70911, DE91 010791.
[50] M.T. Leccia, M.J. Richard, J.C. Bean, H. Faure, A.M. Monjo, J. Cadet, P. Amblard, A. Favier, Protective effect of selenium and zinc on UV-A damage in human skin fibroblasts, Photochem. Photobiol. 58 (1993) 548–553.
[51] C. Nishigori, Y. Hattori, S. Toyokuni, Role of reactive oxygen species in skin carcinogenesis, Antioxid. Redox Signal. 6 (3) (2004) 561–570.
[52] T. Xia, M. Kovochich, J. Brant, M. Hotze, J. Sempf, T. Oberley, C. Sioutas, J.I. Yeh, M.R. Wiesner, A.E. Nel, Comparison of the abilities of ambient and manufactured nanoparticles to induce cellular toxicity according to an oxidative stress paradigm, Nano Lett. 6 (2006) 1794–1807.
[53] E. Corsini, V. Galbiati, D. Nikitovic, A.M. Tsatsakis, Role of oxidative stress in chemical allergens induced skin cells activation, Food Chem. Toxicol. 61 (2013), http://dx.doi.org/10.1016/j.fct.2013.02.038.
[54] L.L. Liu, L.S. He, Y. Xu, Z. Han, Y.X. Li, J.L. Zhong, X.R. Guo, X.X. Zhang, K. Ming Ko, P.Y. Qian, Caspase-3-dependent apoptosis of citreamicin ε-induced HeLa cells is associated with reactive oxygen species generation, Chem. Res. Toxicol. 26 (7) (2013) 1055–1063.
[55] S. Alarifi, D. Ali, Mechanisms of multi-walled carbon nanotubes-induced oxidative stress and genotoxicity in mouse fibroblast cells, Int. J. Toxicol. 34 (3) (2015) 258–265.
[56] M.H. Mamat, Z. Khusaimi, M.Z. Musa, M.F. Malek, M. Rusop, Fabrication of ultraviolet photoconductive sensor using a novel aluminium-doped zinc oxide nanorod-nanoflake network thin film prepared via ultrasonic-assisted sol-gel and immersion methods, Sens. Actuators A Phys. 171 (2011) 241–247.
[57] P. Ghaderi-Sheikhi Abadi, M. Salavati-Niasari, F. Davar, Hydrothermal synthesis and optical properties of antimony sulfide micro and nano-size with different morphologies, Mater. Lett. 71 (2012) 168–171.
[58] Z.Y. Jiang, Q. Kuang, Z.X. Xie, L.S. Zheng, Syntheses and properties of micro/nanostructured crystallites with high-energy surfaces, Adv. Funct. Mater. 20 (2010) 3634–3645.
[59] N. Talebian, S.M. Amininezhad, M. Doudi, Controllable synthesis of ZnO nanoparticles and their morphology-dependent antibacterial and optical properties, J. Photochem. Photobiol. B 120 (2013) 66–73.
[60] K. Ando, H. Saito, Z. Jin, T. Fukumra, M. Kawasaki, Y. Matsumoto, Large magneto-optical effect in an oxide diluted magnetic semiconductor $Zn_{1-x}Co_xO$, Appl. Phys. Lett. 78 (2001) 2700–2702.
[61] B. Saha, S. Das, K.K. Chattopadhyay, Electrical and optical properties of Al doped cadmium oxide thin films deposited by radio frequency magnetron sputtering, Sol. Energy Mater. Sol. C 91 (2007) 1692–1697.
[62] T. Xia, Y. Zhao, T. Sager, S. George, S. Pokhrel, N. Li, D. Schoenfeld, H. Meng, S. Lin, X. Wang, M. Wang, Z. Ji, J.I. Zink, L.M. €adler, V. Castranova, Sh. Lin, A.E. Nel, Decreased dissolution of ZnO by iron doping yields nanoparticles with reduced toxicity in the rodent lung and zebrafish embryos, ACS Nano 5 (2011) 1223–1235.
[63] W. Bai, Z.Y. Zhang, W.J. Tian, X. He, Y.H. Ma, Y.L. Zhao, Z.F.J. Chai, Toxicity of zinc oxide nanoparticles to zebrafish embryo: a physicochemical study of toxicity mechanism, J. Nanopart. Res. 12 (2010) 1645–1654.
[64] R.D. Palmiter, Protection against zinc toxicity by metallothionein and zinc transporter 1, Proc. Natl. Acad. Sci. U. S. A. 101 (2004) 4918–4923.